Mon. Not. R. Astron. Soc. **371,** 1777–1792 (2006) doi:10.1111/j.1365-2966.2006.10796.x

The X-ray properties of optically selected $z > 0.6$ clusters in the European Southern Observatory Distant Cluster Survey

O. Johnson,[1⋆] P. Best,[1] D. Zaritsky,[2] D. Clowe,[2] A. Aragón-Salamanca,[3] C. Halliday,[4] P. Jablonka,[5] B. Milvang-Jensen,[6] R. Pelló,[7] B. M. Poggianti,[8] G. Rudnick,[9] R. Saglia,[10] L. Simard[11] and S. White[9]

[1]*SUPA†, Institute for Astronomy, Royal Observatory Edinburgh, Blackford Hill, Edinburgh EH9 3HJ*
[2]*Steward Observatory, University of Arizona, 933 North Cherry Avenue, Tucson, AZ 85721, USA*
[3]*School of Physics and Astronomy, University of Nottingham, University Part, Nottingham NG7 2RD*
[4]*Osservatorio Astrofisico di Arcetri, Largo E. Fermi 5, 50125 Firenze, Italy*
[5]*GEPI CNRS-UMR8111, Observatoire de Paris, section de Meudon, 5 Place Jules Janssen, F-92195 Meudon Cedex, France*
[6]*Dark Cosmology Centre, Niels Bohr Institute, University of Copenhagen, Juliane Maries Vej 30, DK-2100 Copenhagen, Denmark*
[7]*Laboratoire de' Astrophysique, UMR 5572, Observatoire Midi-Pyrenees, 14 Avenue E. Belin, 31400 Toulouse, France*
[8]*Osservatorio Astronomico, vicolo dell' Osservatorio 5, 35122 Padova, Italy*
[9]*Max-Plank-Institute fur Astrophysik, Karl-Schwarschilde-Strasse 1, Postfach 1317, D-85741 Garching, Germany*
[10]*Max-Plank-Institut fur extraterrestrische Physik, Giessenbachstrasses, D-85748 Garching, Germany*
[11]*Herzberg Institute of Astrophysics, National Research Council of Canada, Victoria, BC V93 2E7, Canada*

Accepted 2006 July 13. Received 2006 June 29; in original form 2006 March 6

ABSTRACT

We present *XMM–Newton* observations of three optically selected $z > 0.6$ clusters from the European Southern Observatory (ESO) Distant Cluster Survey (EDisCS), comprising the first results of a planned X-ray survey of the full EDisCS high-redshift sample. The EDisCS clusters were identified in the Las Campanas Distant Cluster Survey as surface brightness fluctuations in the optical sky and their masses and galaxy populations are well described by extensive photometric and spectroscopic observations. We detect two of the three clusters in the X-ray and place a firm upper limit on diffuse emission in the third cluster field. We are able to constrain the X-ray luminosity and temperature of the detected clusters and estimate their masses. We find that the X-ray properties of the detected EDisCS clusters are similar to those of X-ray-selected clusters of comparable mass and – unlike other high-redshift, optically selected clusters – are consistent with the T–σ and L_X–σ relations determined from X-ray-selected clusters at low redshift. The X-ray determined mass estimates are generally consistent with those derived from weak-lensing and spectroscopic analyses. These preliminary results suggest that the novel method of optical selection used to construct the EDisCS catalogue may, like selection by X-ray luminosity, be well suited for identification of relaxed, high-redshift clusters whose intracluster medium is in place and stable by $z \sim 0.8$.

Key words: galaxies: clusters: general – X-rays: galaxies: clusters.

1 INTRODUCTION

Surveys of distant galaxy clusters provide vital information about the development of the Universe on many scales. The evolution of the cluster mass function with redshift is among the key testable predictions of hierarchical cosmologies, whereas the properties of the intracluster medium (ICM) reflect both the physics of baryonic structure formation and the effects of feedback from evolving galaxy populations. The galaxies within dense environments comprise convenient and unique samples in which to study galaxy formation and evolution as well as the dependence of these processes on environment. Additionally, the properties and demographics of active galactic nuclei (AGN) hosted by cluster members may provide insight into the triggering mechanisms of nuclear activity and the role of AGN feedback in the development of host galaxies and the ICM (e.g. Johnson, Best & Almaini 2003; Martini et al. 2006). In recent years, therefore, considerable effort has been devoted to the construction of catalogues of high-redshift clusters which will put statistically significant constraints on the evolution of clusters and cluster galaxy populations from early epochs.

Clusters are commonly identified either through optical/infrared (optical/IR) searches for galaxy overdensities or through X-ray

⋆E-mail: cocj@roe.ac.uk
†Scottish Universities Physics Alliance

detection of the intracluster gas. Optical/IR studies have the advantage of efficiently surveying very large volumes of sky, but have traditionally been marred by a high rate of spurious identifications of line-of-sight superpositions. While modern surveys utilizing optimal colour filters (e.g. Postman et al. 1996; Gladders & Yee 2005) can substantially mitigate this shortcoming, it is increasingly problematic at high redshift where the colour distinction between member and non-member galaxies decreases. In contrast, X-ray observations allow unambiguous identification of clusters over well-defined survey areas as well as direct measurement of the properties of the ICM (e.g. Gioia et al. 1990; Rosati et al. 1998). Recent observations with the *Chandra* and *XMM–Newton* observatories have detected clusters to $z \sim 1.4$ (e.g. Mullis et al. 2005), and surveys currently underway with these instruments promise systematic exploration of the $z > 1$ cluster population (e.g. Romer et al. 2001; Pierre et al. 2003; Green et al. 2004). However, selection based on detection of a luminous ICM may significantly bias these samples towards the inclusion of only the most-massive, gas-rich, virialized clusters and/or systems in which shocks elevate the X-ray temperature and flux.

A critical issue in the interpretation of ongoing cluster studies, then, is the quantification of the biases inherent in the various cluster selection techniques and their dependence on both detection wavelength and redshift. Several authors have recently addressed the question of whether X-ray and optical detection techniques are equal probes of the cluster population (e.g. Donahue et al. 2001, 2002), generally concluding that they are not. At lower redshift, it appears that optical surveys may be able to detect less-massive and/or less-evolved systems. For example, Plionis et al. (2005) and Basilakos et al. (2004) investigated the low X-ray luminosity of many optically selected cluster candidates in Sloan Digital Sky Survey data and concluded that the optical candidates are poor groups and/or structures which have not yet virialized. Towards higher redshift, however, there is evidence that the properties of massive, optically selected clusters may differ systematically from those of X-ray-selected clusters of comparable mass. Several *ROSAT* observations of optically selected samples of clusters at $z \sim 0.5$ suggest that they have consistently low X-ray luminosities for their apparent optical richness compared to X-ray-selected samples (e.g. Bower et al. 1994; Castander et al. 1994; Holden et al. 1997). Lubin, Mulchaey & Postman (2004) have obtained *Chandra* observations of optically selected clusters at $z = 0.76$ and 0.90 and reported that both exhibit X-ray luminosity and temperature which are low for their measured velocity dispersion according to the low-redshift L_X–σ and T–σ scaling relations. Similarly, a *Chandra* survey of clusters at $0.6 < z < 1.0$ selected by the Red-Sequence Cluster Survey (RCS; Gladders & Yee 2005) found them to be cooler, less luminous, and less centrally condensed than X-ray-selected clusters of similar optical richness (Hicks et al. 2004).

The physical implications of the variation in the X-ray properties of optically and X-ray-selected high-redshift cluster samples may be significant, but are currently poorly understood. If the optically selected sources are representative of the high-redshift cluster population in general, their deviation from the X-ray–optical scaling relations would indicate significant evolution of the ICM since $z \sim 0.8$. That this evolution is not apparent in X-ray-selected samples might suggest that X-ray luminosity is, indeed, a biased and limited indicator of the cluster population at high redshift. On the other hand, as suggested by Bower et al. (1997) and Lubin et al. (2004), optical cluster surveys at high redshift may, like those at lower redshift, simply be able to select less fully evolved systems. At redshifts where hierarchical structure formation models suggest that clusters should still be in the process of collapsing along filaments, significant populations of massive protocluster systems may exist which have not yet developed a luminous ICM. The masses implied by the velocity dispersions in such collapsing systems may be inflated by non-equilibrium dynamics, whereas the properties of the ICM, particularly in lower-mass structures, may be significantly affected by non-gravitational heating by stellar winds, cluster AGN, and/or substructure merging. If the optically selected cluster surveys at high redshift have preferentially selected these forming systems, their deviation from the L_X–σ and T–σ relations would not necessarily imply the evolution in the ICM properties of the general cluster population or indicate a strong bias in X-ray-selected samples of virialized clusters.

Developing a physical understanding of the variation between X-ray and optically selected high-redshift cluster samples is clearly vital to know how well these survey techniques reflect the underlying mass distribution, and may also provide valuable information about the mechanisms and time-scales of mass congregation and ICM heating in forming structures. Unfortunately, however, there are currently very few high-redshift clusters which have been extensively studied at both optical and X-ray wavelengths. In addition, the vast majority of detailed X-ray measurements of high-redshift clusters to date have been of massive X-ray-selected systems which will evolve to populate the highest-mass tip of the present-day cluster population. To address these issues, we are conducting an X-ray survey of clusters drawn from the high-redshift sample of the European Southern Observatory (ESO) Distant Cluster Survey (EDisCS; White et al. 2005), a uniquely well-studied set of optically selected $z > 0.6$ clusters. As EDisCS clusters were first identified in the Las Campanas Distant Cluster Survey (LCDCS; Gonzalez et al. 2001) based on optical intracluster light within a compact spatial filter, the survey is tuned to detect dynamically relaxed systems independent of their X-ray flux. The mass and dynamical state of structures in the EDisCS fields are known from well-determined velocity dispersions (Halliday et al. 2004; Milvang-Jensen et al., in preparation) as well as weak-lensing mass reconstructions (Clowe et al. 2006) for each cluster. Finally, the mass distribution of the EDisCS sample differs significantly from that of existing X-ray-selected samples, extending to much lower masses and, when evolved to $z = 0$, matching the distribution of nearby clusters significantly better (Poggianti et al. 2006).

In this paper, we present *XMM–Newton* observations of the first three EDisCS clusters. We describe the EDisCS programme and the target clusters in Section 2 and the reduction and analysis of the X-ray data in Section 3. In Section 4, we report on the X-ray properties of each cluster in turn before discussing the ensemble results in Sections 5 and 6 and summarizing our findings in Section 7. Throughout this paper, we assume a Λ cold dark matter (ΛCDM) cosmology with $\Omega_m = 0.3$, $\Omega_\Lambda = 0.7$, and $H_0 = 70$ km s^{-1} kpc^{-2}. Unless specified otherwise, errors throughout are quoted at the 90 per cent confidence level.

2 THE EUROPEAN SOUTHERN OBSERVATORY DISTANT CLUSTER SURVEY

The principal goal of EDisCS is the quantitative analysis of the evolution of cluster galaxy populations since $z \sim 0.9$. Targets were drawn from the LCDCS (Gonzalez et al. 2001), in which cluster candidates were detected as low surface brightness peaks in source-subtracted drift-scan observations of a 90° by 1.°5 strip of sky and assigned estimated redshifts from the apparent magnitude of the brightest cluster galaxy (BCG). The EDisCS 'mid-z' and 'hi-z'

Table 1. Properties of EDisCS clusters observed with *XMM–Newton*. Listed for each cluster are: position of the BCG, cluster redshift, the number of spectroscopically confirmed members, spectroscopically determined velocity dispersion, and estimated cluster mass. Mass estimates are derived from the weak-lensing analysis of Clowe et al. (2006) and quoted at a radius of 1 Mpc. No significant peak was detected in the weak-lensing mass reconstruction map for Cl1040−1155; the mass estimate quoted for this cluster is a 2σ upper limit. All other values are from Halliday et al. (2004).

Cluster	RA (J2000)	Dec. (J2000)	Redshift	N	σ (km s^{-1})	$M_{\rm lens}$ (10^{14} M$_\odot$)
Cl1216−1201	12 16 45.1	−12 01 18	0.79	66	1018^{+73}_{-77}	6.2
Cl1054−1145	10 54 24.5	−11 46 20	0.70	48	589^{+78}_{-70}	3.7
Cl1040−1155	10 40 40.4	−11 56 04	0.70	30	418^{+55}_{-46}	<2.2

samples are comprised of 10 bright LCDCS candidates at $z \sim 0.5$ and $\sim$0.8, respectively, for which VLT imaging could confirm the presence of an apparent cluster with a possible red sequence (Gonzalez et al. 2002). For these clusters, we have obtained a high-quality, homogenous data set of deep optical and near-IR photometry, deep optical spectroscopy, wide-field imaging, and high-resolution *Hubble Space Telescope*/Advanced Camera for Surveys (*HST*/ACS) imaging (see White et al. 2005, and references therein for a full description of the EDisCS data). Multiobject spectroscopic observations have identified between 10 and 70 members in each cluster, yielding robust measurements of cluster velocity dispersions as well as indications of cluster substructure (Halliday et al. 2004; Milvang-Jensen et al., in preparation). In addition, photometric redshifts based on both optical and IR colours are available across the cluster fields (Pelló et al., in preparation) and a weak-shear lensing analysis of the photometric data has provided mass reconstructions over the $\sim$6.5 × 6.5-arcmin^2 VLT/FORS2 field of view (FOV) (Clowe et al. 2006).

We plan a detailed X-ray survey of nine EDisCS cluster fields with a redshift range of $0.6 \lesssim z \lesssim 0.8$ (median $z = 0.7$). Our X-ray sample is comprised of eight of the 10 'hi-z' clusters and one 'mid-z' cluster with spectroscopically confirmed $z \gtrsim 0.6$. The number of spectroscopically confirmed members, N, in the target clusters ranges from 14 to 66 (median $N = 22$) and implies a range in velocity dispersion of 320 km s^{-1} $\lesssim \sigma \lesssim$ 1020 km s^{-1} (median $\sigma \simeq$ 570 km s^{-1}). Four additional $z \gtrsim 0.6$ structures will be serendipitously observed in these fields, extending the sample to higher redshift ($z_{\rm max} \simeq 0.96$) and lower velocity dispersion ($\sigma_{\rm min} = 242$ km s^{-1}). In this paper, we present *XMM* observations of the first three clusters: Cl1216−1201, Cl1054−1145, and Cl1040−1155. These fields were chosen for this initial X-ray study from among the five presented in the first EDisCS spectroscopic paper by Halliday et al. (2004) and cover a broad range in velocity dispersion. Their optical properties are discussed in turn in Section 4 and summarized in Table 1.

3 X-RAY DATA

We obtained *XMM–Newton* observations of the Cl1216−1201, Cl1054−1145, and Cl1040−1155 fields with scheduled exposure times of $\sim$30 ks each. The three detectors comprising the European Photon Imaging Camera (EPIC) – two Metal Oxide Semiconductor (MOS) CCDs and one pn camera – were all functioning nominally throughout these exposures, which were taken in Full Window mode through the medium filter. Details of the observations and their reduction are summarized in Table 2.

3.1 Data preparation

We reduced the raw data using version 6.0.0 of the *XMM* Science Analysis System (SAS). We identified periods of background flaring in 7–15 keV light curves and removed them; the remaining usable exposures are listed in Table 2. We applied the standard recommended filters, excluding events with PATTERN >12 or energies outwith the 0.2–15 keV range. To create event lists suitable for spectral analysis, we used more conservative filters, removing pn events with PATTERN >4 and all events with FLAG ≠ 0. We also chose these conservative filters in pn imaging analysis as they significantly reduce visible artefacts, particularly at soft energies.

We made images for each of the EPIC cameras in the full (0.5–8 keV), soft (0.5–2 keV), and hard (2–8 keV) bands by binning the filtered events into 2 arcsec pixels. We calculated energy conversion factors (ECFs) for these bands from appropriate calibration data as described in XMM Survey Science Centre memo SSC-LUX_TN-0059, Issue 3.0, and listed them in Table 3. This procedure adopts a power-law spectrum with a photon index $\gamma = 1.7$ and an absorbing column of 3×10^{20} cm^{-2}. We generated exposure maps for these images with the EEXPMAP task, which assumes monochromatic spectra with energies at the mid-point of each band.

Table 2. Properties of *XMM* observations of three EDisCS clusters. Listed for each cluster are: observation date, observation ID, position of *XMM* aim-point, scheduled exposure time, 7–15 keV background rate above which flares were filtered for pn and MOS, and remaining usable exposure time for pn and MOS.

Cluster	Date	Observation ID	RA (J2000)	Dec. (J2000)	Exposure time (ks)	Background rate (counts s^{-1})		'On' time (ks)	
						MOS	pn	MOS	pn
Cl1216−1201	2003 July 6	0143210801	12 16 45.0	−12 01 17	33.9	0.8	3.0	27.7	25.5
Cl1054−1145	2004 December 29–30	0201330201	10 54 21.2	−11 46 18	34.6	0.8	2.4	31.6	27.3
Cl1040−1155	2005 May 19	0201330101	10 40 41.6	−11 55 51	33.9	0.6	2.2	31.6	25.5

Table 3. *XMM* ECFs for the full, soft, and hard bands, in units of 10^{11} counts cm^2 erg^{-1}. These values are calculated from appropriate calibration data as described in the text.

Band (keV)	MOS 1 ECF	MOS 2 ECF	pn ECF
0.5–8.0	1.067	1.071	3.396
0.5–2.0	1.980	1.977	6.596
2.0–8.0	0.510	0.518	1.457

We combined EPIC images by summing the individual instrument images after setting all pixels with zero exposure to zero counts. We generated merged exposure maps by multiplying the individual exposure maps by the instrumental effective area before summing. While these maps are sufficient to 'flat-field' the count images for the purposes of source detection and rough spatial analysis, they are not accurate enough to provide reliable fluxes and therefore are not used in the derivation of source properties.

3.2 Imaging analysis

We adaptively smoothed the full-band images using the CSMOOTH tool available from the Chandra X-ray Centre so that only features locally significant at the 99 per cent level remain visible. We identified point sources in the unsmoothed full-band images as detailed in Section 3.4 and excised all events within the 3σ detection ellipses.

We made radially averaged surface brightness distributions of the diffuse emission by summing exposure-corrected counts from the source-free images in annuli. We summed the source counts in 4-arcsec annuli to radii of 80 arcsec (598 kpc at $z = 0.79$ and 571 kpc at $z = 0.70$), measured the background level between 80 and 100 arcsec, and subtracted it. We modelled the distributions with a standard β-function of the form

$$S(r) = S_{\rm o}\left[1 + \left(\frac{r}{r_{\rm c}}\right)^2\right]^{-3\beta+(1/2)}, \quad (1)$$

where $S(r)$ is the surface brightness at radius r, $S_{\rm o}$ is the central surface brightness, $r_{\rm c}$ is the core radius, and β is the slope at large radii. We minimized the fits in the CIAO SHERPA package using the Chi Gehrels statistic (Gehrels 1986) and estimated confidence intervals through projection of the statistic surface using the PROJ task. We note that this approach does not consider the extent of the *XMM* point spread function (PSF).

3.3 Spectral analysis

As discussed at length in Lumb et al. (2002), Read & Ponman (2003), and Nevalainen, Markevitch & Lumb (2005), the complex spectral and spatial variation of the *XMM* background presents a significant challenge in analysis of extended and/or faint sources. The background flux is comprised of an unvignetted particle component exhibiting sharp spectral and spatial structure as well as a vignetted cosmic background which is approximately constant across the FOV. In the current analysis, we compared the result of background subtraction using: (i) single background regions, (ii) multiple background regions, and (iii) the Read & Ponman (2003) background maps, following the prescription of Arnaud et al. (2002). The best-fitting parameters obtained using all three methods were consistent within the uncertainties, which were substantial for method (iii) due to the poor statistical quality of the spectra. The results presented are based on the spectra constructed using multiple background regions.

We extracted source and background spectra from point-source-free event lists within optimized extraction regions estimated from the spatial analysis described above. We created spectra and response files for each of the three EPIC cameras, using the standard SAS tools, and fitted them simultaneously to an absorbed MEKAL model of hot, diffuse gas emission (Mewe, Lemen & van den Oord 1986; Mewe, Gronenschild & van den Oord 1985; Kaastra 1992; Liedahl, Osterheld & Goldstein 1995) within the XSPEC package. In fitting the spectra, we excluded the 1.45–1.55 keV band to avoid highly variable Al K florescence associated with the detectors and detector housings, as suggested in Nevalainen et al. (2005), and we restricted the fit to energies above 0.5 and below 8 keV. Prior to fitting, we grouped the spectra such that there are a minimum of 25 counts in each bin to allow the use of the χ-squared statistic. We again estimated confidence levels from the statistic surface.

3.4 Detection and characterization of point sources

We detected X-ray sources in the 0.5–8 keV full-EPIC images using versions of the WTRANSFORM and WRECON algorithms distributed by the Chandra X-ray Center (Freeman et al. 2002), using wavelet scales of $\sqrt{2}$, $2\sqrt{2}$, 4, $4\sqrt{2}$, 8, $8\sqrt{2}$ and 16 pixels. We set the significance threshold conservatively at 1×10^{-8}, such that less than one false source is expected per field. We further limited the final source lists to include only sources with greater than 10 counts and a source significance value of $\sigma_{\rm src} > 4$, where $\sigma_{\rm src}$ is defined in terms of source counts, $C_{\rm src}$, and background counts, $C_{\rm bkg}$, as $\frac{C_{\rm src}}{1+\sqrt{0.75+C_{\rm bkg}}}$.

We determined source counts, background counts and mean exposure values for each detector and each band within apertures with 8 arcsec radii. We obtained background counts from the output WTRANSFORM background image and converted net counts within the aperture to total net counts by dividing by the fractional encircled energy (EE) within the aperture. The EE is a function of off-axis angle and was determined using the Extended Accuracy Model of the *XMM* PSF. We derived instrumental fluxes by dividing the total counts by the mean exposure value and the appropriate ECF. Fluxes quoted in this paper are an error-weighted average of the fluxes measured by each instrument. Hardness ratios are defined as $HR = \frac{H-S}{H+S}$ where H and S are the 0.5–2 and 2–8 keV error-weighted count-rates given by each instrument, after background subtraction and exposure correction. The on-axis, full-band flux limit for 3σ detection of point sources was $\sim 1 \times 10^{-15}$ erg s^{-1} cm^{-2} for all three observations. Catalogues of the X-ray point sources in each field are given in Appendix A (Supplementary Material section, below) and in machine-readable form at the Centre de Donne´es astronomiques de Strasbourg (CDS).

3.5 Astrometric calibration and optical counterparts

We identified optical counterparts to the X-ray point sources on astrometrically corrected 60-min exposures obtained with the Wide-Field Imager (WFI) at the ESO/MPG 2.2-m telescope which cover the full *XMM–Newton* FOV (Clowe et al., in preparation). We used the ASTROM algorithm to correct the astrometry of the X-ray data by performing six-coefficient fits to the positions of bright X-ray sources with unambiguous optical counterparts in I-band WFI images. The values of rms of these fits were $\sim$1.5 arcsec for all fields, consistent with the published positional accuracy of *XMM*. We then identified candidate optical counterparts for all X-ray sources through comparison of the X-ray and I-band catalogues, using a

likelihood ratio technique similar to that employed by Sutherland & Saunders (1992) and Rutledge et al. (2000). For each X-ray source, we consider the catalogue of M optical counterparts and define the likelihood ratio, LR, of the ith candidate counterpart as

$$LR_i = \frac{\exp\left(-r_i^2/2\sigma_i^2\right)}{\sigma_i^2 N(< I_i)},$$

where r_i is the distance between the X-ray source and the candidate, σ_i is the uncertainty in the source position, and $N(< I_i)$ is the number of optical sources with I-band magnitude less than or equal to that of the candidate. To estimate the reliability of source association as a function of LR, we randomly shift the optical catalogue and recalculate the likelihoods, repeating the procedure 5000 times to obtain a smooth histogram of LR values for false associations. The reliability, R, of the ith optical candidate is then given by

$$R_i = 1 - N_{\rm bkg}(\geqslant LR_i),$$

where $N_{\rm bkg}(\geqslant LR_i)$ is the number of false associations with LR greater than or equal to that of the candidate. We then calculate both the probability that there is no unique counterpart to the X-ray source:

$$P_{\rm none} = \frac{\prod_{j=1}^{M}(1 - R_j)}{S}$$

and the probability that the ith candidate is the true counterpart to the X-ray source:

$$P_{{\rm id},i} = \frac{\frac{R_i}{1-R_i}\prod_{j=1}^{M}(1 - R_j)}{S}.$$

The normalization, S, is found by summing over the full set of possibilities:

$$S = \sum_{i=1}^{M}\frac{R_i}{1-R_i}\prod_{j=1}^{M}(1 - R_j) + \prod_{j=1}^{M}(1 - R_j).$$

Catalogues of the optical counterparts determined from the WFI data are given in Appendix B (Supplementary Material section, below) and in electronic form at the CDS. Multiband optical properties of the candidate optical counterparts within the VLT FOV are given in Tables B4, B5, and B6.

3.6 Identifying possible cluster AGN

In support of the EDisCS science goal of examining evolution in cluster galaxy populations, we plan a survey of AGN hosted by EDisCS cluster members. In this initial paper, we use the multiband photometric and spectroscopic data available for X-ray sources detected in the central regions of the cluster fields to identify possible cluster AGN. Photometric redshifts for all galaxies in the FORS fields have been determined using two independent photometric redshift codes (Bolzonella, Miralles & Pelló 2000; Rudnick et al. 2001, 2003) and are presented in Pelló et al. (in preparation). Each code returns its own probability histogram, $P(z)$, which is normalized to unity over $0 < z < 2$. The probability of cluster membership, $P_{\rm mem}$, is then defined as the integrated probability that $z_{\rm phot} = z_{\rm cluster} \pm 0.1$. If both codes return an integrated probability greater than a threshold value determined through analysis of the spectroscopic identifications in each field, galaxies are flagged as possible cluster members (see Pelló et al., in preparation, for details). In addition, the BOLZONELLA code also returns a best-fitting redshift using a quasar template, $z_{\rm QSO}$. We present X-ray sources with optical properties plausibly consistent with cluster membership in Sections 4.1.4, 4.2.4 and 4.3.2 below, but caution that these candidates for further study have been selected liberally.

4 ANALYSIS OF INDIVIDUAL EUROPEAN SOUTHERN OBSERVATORY DISTANT CLUSTER SURVEY FIELDS

4.1 Cl1216−1201

Cl1216−1201 at $z = 0.79$ is among the richest and highest-redshift EDisCS clusters, with 66 spectroscopically confirmed cluster members yielding a velocity dispersion of 1018^{+73}_{-77} km s^{-1} (Halliday et al. 2004). The photometric data indicate a strong red sequence and a well-defined sequence of bluer, presumably star-forming, galaxies (White et al. 2005). The mass reconstruction of the field indicates a mass peak coincident with both the BCG and the peak in galaxy density (Clowe et al. 2006), and there is also a strongly lensed arc associated with the cluster. Examination of the three-dimensional distribution of the cluster galaxies reveals substructures, with one component centred on the BCG and a second extending to the north-east (Halliday et al. 2004). Corresponding filamentary structures are evident at moderate significance levels in the lensing map.

4.1.1 Cl1216−1201: spatial analysis

We show X-ray contours overlaid on an I-band image of the central region of the Cl1216−1201 field in Fig. 1. An extended source (Cl1216_X46) is evident at the *XMM* aim-point, coincident with a dense concentration of spectroscopically confirmed cluster members which includes the BCG. A second diffuse component (Cl1216_X62), hereafter Cl1216-South, lies roughly 3.5 arcmin to the south-west of the *XMM* aim-point and is significantly fainter and less centrally concentrated than the emission at the aim-point (see Section 4.1.5). The bright compact source (source Cl1216_X9) embedded in the main cluster emission ∼40 arcsec to the west is coincident with a large, bright ($I = 18.2$) foreground elliptical with a photometric redshift of ∼0.6. Where the Cl1216−1201 contours are unaffected by the point-source flux, they appear regular and round, suggesting that the main component of the cluster gas is reasonably relaxed despite the substructure detected in the galaxy distribution and mass map. Fig. 2 shows the smoothed X-ray flux in grey-scale with contours from the weak-lensing mass reconstruction of the field overlaid by Clowe et al. (2006). The weak-lensing peak is offset slightly to the east of the X-ray peak and the BCG, and the contours extend along a NNE–SSW axis. The FOV of the lensing observations does not extend far enough to the south to include Cl1216-South.

A radially averaged surface flux profile of the main cluster component centred on the peak of the X-ray emission ($\alpha = 12^{\rm h}16^{\rm m}45\overset{\rm s}{.}4$, $\delta = -12^\circ01'15''$[$J2000$]), is shown in Fig. 3 (left-hand panel). The best-fitting β-model parameters were $r_{\rm c} = 159 \pm^{20}_{18}$ kpc and $\beta = 0.68 \pm^{0.06}_{0.05}$. We note that these errors, obtained by projection of the χ^2 surface along the parameter axis, underestimate the true uncertainty in β and $r_{\rm c}$ due to the correlation of these parameters, as shown in Fig. 3 (right-hand panel). Additionally, an upward kink in the data at ∼40 arcsec suggests that residual wings of the nearby point source may contaminate the cluster emission beyond this radius.

As there were sufficient counts, we also modelled the surface brightness distribution in two dimensions. Using the CIAO SHERPA package, we fit the full-band image of the cluster emission with a model comprised of a two-dimensional β-model – which includes eccentricity (e) and position angle (θ) terms to allow for non-sphericity – multiplied by the exposure map and convolved with a model of the *XMM* PSF. We used the SAS CALVIEW tool to

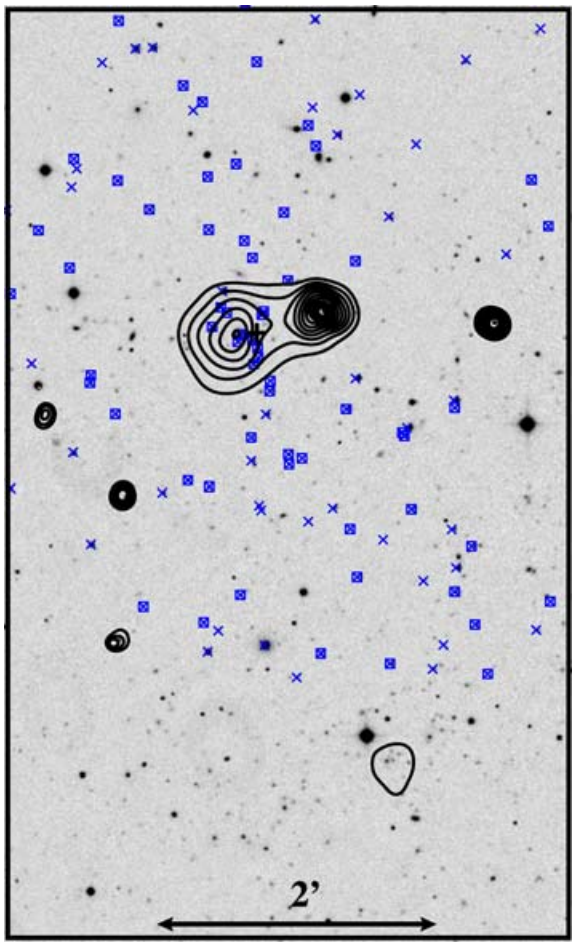

Figure 1. X-ray contours overlaid on an *I*-band image of the central region of the Cl1216−1201 field. The small 'x' symbols indicate sources for which spectra have been obtained; the squares indicate spectroscopically confirmed cluster members. North is up, east is to the left-hand side, and the *XMM* aim-point is indicated by the cross. The diffuse sources to the north are the main Cl1216−1201 component (east) and contaminating point source (west); the fainter source to the south-west is Cl1216-South. The edge of the FOV of the spectroscopic observations lies just to the north of the southern component.

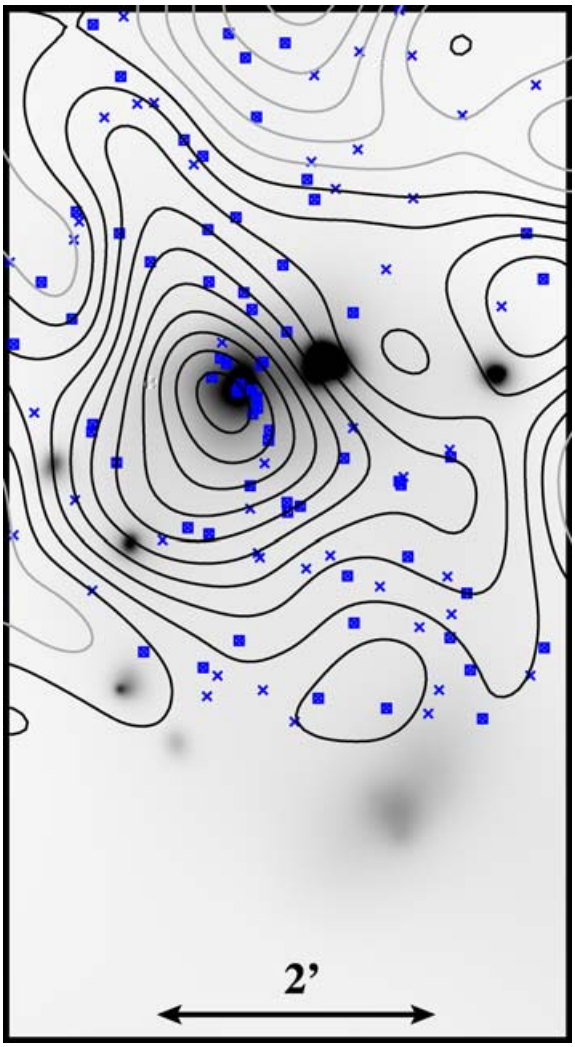

Figure 2. Adaptively smoothed 0.5–8 keV X-ray image of the central region of the Cl1216−1201 field with the Clowe et al. (2006) weak-lensing mass reconstruction of the field overlaid. Contour intervals are $\sim 1 \times 10^8$ $M_\odot$ kpc^{-2} relative to the local mean, with negative contours shown in light grey. The crosses indicate sources for which spectra have been obtained; the squares indicate spectroscopically confirmed cluster members. North is up and east is to the left-hand side. The edge of the lensing map lies just to the north of the southern component.

generate a model of the PSF at 2 keV. (The *XMM* PSF is not strongly energy-dependent at energies less than 5 keV and off-axis angles less than 4 arcmin.) We selected the Medium Accuracy model, which is the only two-dimensional calibration of the *XMM* PSF currently available, but note that it is known to provide a less-accurate description of the radially averaged PSF than the Extended Accuracy model (see *XMM–Newton* Calibration Access and Data Handbook, memo XMM-PS-GM_20 Issue 2.1). We rebinned the images, exposure maps, and model PSF into a common 2.2 arcsec pixel scale and normalized exposure maps to their maximum value to retain the statistics of the counts image as much as possible.

The bright point source within the fit region was represented as a δ-function and added to the model prior to the addition of instrumental effects. We also included a constant background level, which we determined from a fit to a source-free region and fixed. Neither the source-free background nor the exposure map, excluding chip gaps, varied significantly over the fitted region. The low count-rate per bin required minimization via the Cash statistic (Cash 1979), and we computed confidence intervals from the statistic surface, using the region projection task (RPROJ) within SHERPA. The best-fitting model was spherical ($e = \theta = 0$) with $\beta = 1.2 \pm^{0.5}_{0.3}$ and $r_c = 97 \pm^{28}_{18}$ kpc. We show the radially averaged profiles of the raw counts image, the best-fitting model, and the model components in Fig. 4.

The deviation of the model from the data near to the point-source peak is likely to result from differences between the Medium Accuracy model *XMM* PSF and the observed profile of the point source. As the source is nearly on-axis and the PSF should be approximately radially symmetric, we attempted to obtain a better fit using the radially averaged High and Extended Accuracy models. None of the model PSFs was found to sufficiently fit the peak of the point source, but choice of PSF model did significantly alter the best-fitting parameters of the cluster profile. This uncertainty precludes rigorous constraint of the cluster properties from the two-dimensional fits; the best-fitting β and r_c parameters from these fits cannot be used to accurately model the cluster.

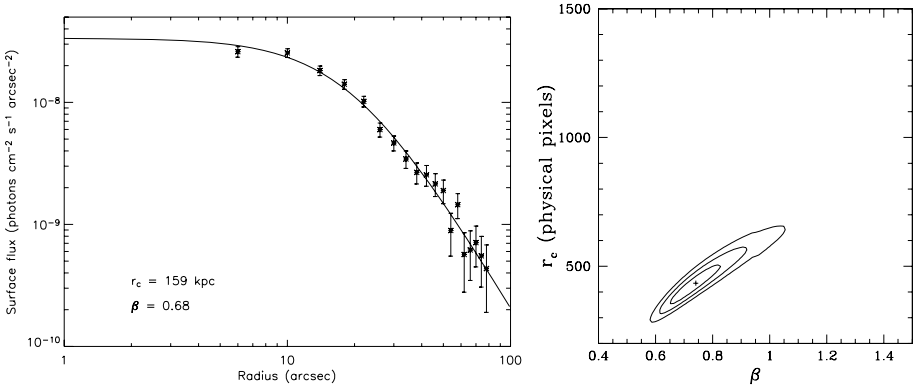

Figure 3. Left-hand panel: radial surface flux profile for Cl1216−1201 obtained by masking point sources and summing exposure-corrected, background-subtracted counts within annuli. Imperfect subtraction of a contaminating point source may be evident beyond 40 arcsec. Right-hand panel: corresponding constraints on β and r_c. The r_c axis is in *XMM* physical pixels which are 0.05 arcsec on a side. The contours mark 1, 2 and 3σ levels.

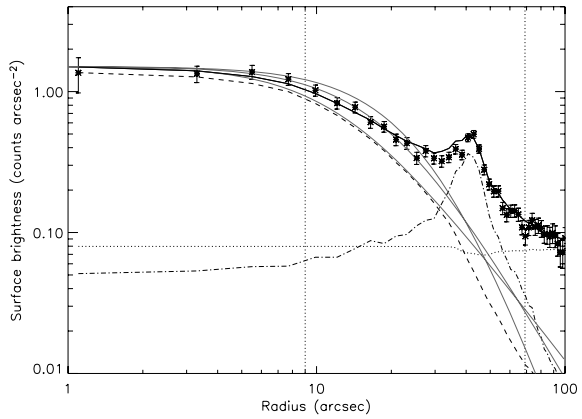

Figure 4. Radial surface brightness profile for Cl1216−1201 obtained through two-dimensional modelling of the uncorrected counts image. The best-fitting model (solid curve) is comprised of cluster emission (dashed curve), a nearby point source (dot–dashed curve), and a constant background level (dotted curve). The grey curves indicate the best-fitting relation from the one-dimensional modelling (see Fig. 3) and relations at the extreme of the 3σ errors on r_c and β as indicated in Fig. 3. The vertical dotted lines mark the region around the point source which was excluded from the one-dimensional profile.

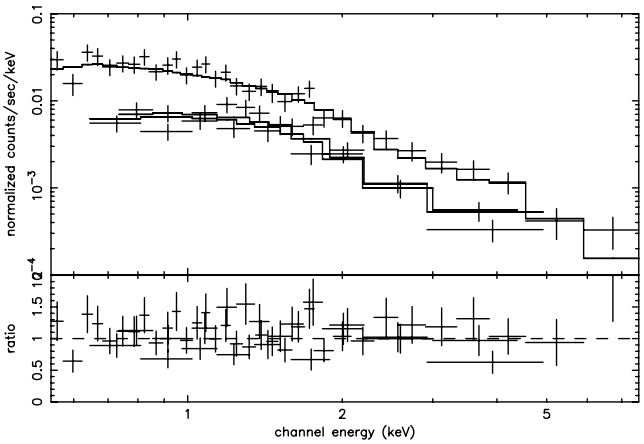

Figure 5. X-ray spectra of Cl1216−1201 extracted from the MOS (lower points) and pn (upper points) cameras and best-fitting thermal emission model (histograms). Residuals are shown in the lower panel.

The two-dimensional model is useful, however, in examining the extent of point-source contamination in the one-dimensional fit. Regardless of which PSF model is used, the point-source wings remain above the background level to radii of nearly 25 arcsec. By comparison, the region excluded by the 3σ ellipse produced by WTRANSFORM for this source has a radius of ∼30 arcsec. While the outmost bins beyond ∼70 arcsec in Fig. 4 indicate that some fraction of emission in the point-source wings may be mistakenly ascribed to the cluster in a one-dimensional fit, it is clear that the majority of the point-source emission is successfully removed within the 3σ ellipse. In addition, the two-dimensional fit demonstrates that the cluster emission is roughly spherical. The one-dimensional fit should therefore provide a good estimate of the spatial distribution of the cluster emission.

4.1.2 Cl1216−1201: spectral analysis

We extracted spectra of the cluster emission for the three EPIC cameras within circles centred on the *XMM* aim-point with radii of 40 arcsec, as the imaging analysis indicates that this region is clearly dominated by cluster emission. Background counts were measured in five circular regions with radii of 115 arcsec centred within 7 arcmin of the aim-point and avoiding Cl1216-South. The source aperture yielded 1503 counts where 194 are expected from the background. Based on the properties of the bright point sources and the Medium Accuracy model of the *XMM* PSF, we estimate that <5 per cent of the extracted counts could be contamination from the wings of the bright neighbouring source. As we have extracted the spectrum only where the cluster emission appears clearly dominant (see Fig. 4), we expect the contamination to be negligible. Use of a less-conservative extraction region with a radius of 115 arcsec was also examined. The spectrum from the larger extraction region yielded a consistent estimation of the cluster temperature, but exhibited more structure due to background emission and indicated an aperture-corrected luminosity which was ∼20 per cent higher than that quoted below, likely due to the incomplete removal of the point-source wings.

The spectra were fitted to an absorbed MEKAL model with the absorption fixed at the Galactic value of 4.1×10^{20} cm^{-2} and the metallicity fixed at 0.3 solar. The best-fitting model (reduced $\chi^2 = 1.0$) is plotted over the data in Fig. 5 and yields a temperature of $4.8 \pm ^{0.8}_{0.7}$ keV, a full-band luminosity of $L_{0.5-8\,\mathrm{keV}} = 2.5 \pm 0.2 \times$

10^{44} erg s^{-1}, and a bolometric luminosity of $L_{\rm bol} = 3.0 \pm 0.2 \times 10^{44}$ erg s^{-1} within the extraction radius. If the emission follows the one-dimensional β profile derived above, the spectral radius encloses 57 per cent of the total cluster luminosity, which extrapolates to $\sim 5 \times 10^{44}$ erg s^{-1}.

4.1.3 Cl1216−1201: mass estimate

Under the assumptions that a cluster is spherically symmetric, in hydrostatic equilibrium, and is well described by an isothermal β profile, and adopting a mean molecular mass of 0.59 times the proton mass, the total gravitating mass of the cluster at a given radius, $M(r)$, can be expressed in terms of the temperature of the gas, T, and the core radius, $r_{\rm c}$, and slope, β, of the surface brightness profile:

$$M(r) = 1.13 \times 10^{14} \beta\, T\, r\, \frac{(r/r_{\rm c})^2}{1 + (r/r_{\rm c})^2}, \quad (2)$$

where T is in keV, r and $r_{\rm c}$ are in Mpc, and M is in $\mathrm{M}_{\odot}$ (Evrard, Metzler & Navarro 1996). The best-fitting values derived from the spectral fit and the best-fitting one- and two-dimensional surface brightness models give masses within 1 Mpc of $\sim 4 \times 10^{14}$ and $\sim 7 \times 10^{14}\,\mathrm{M}_{\odot}$, respectively. The range of these values illustrates the scale of the uncertainty in the X-ray derived mass estimate. In comparison, assuming that the mass distribution is reasonably approximated by a singular isothermal sphere – that is, $M(r) = 2\sigma_{\rm v}^2 r/G$, where $\sigma_{\rm v}$ is the velocity dispersion in km s^{-1} – the weak-lensing analysis of Clowe et al. (2006) implies a mass within 1 Mpc of $(5.4 \pm 1.2) \times 10^{14}\,\mathrm{M}_{\odot}$, where the stated errors are 1σ. The X-ray and weak-lensing mass estimates are therefore broadly consistent. A further comparison can be made with the system mass estimated from the velocity dispersion of cluster members, as in Finn et al. (2005):

$$M_{\rm sys} = 1.2 \times 10^{15} \left(\frac{\sigma}{1000\ \mathrm{km\ s^{-1}}} \right)^3 \frac{1}{\sqrt{\Omega_\Lambda + \Omega_0 (1+z)^3}}\, h^{-1}\, \mathrm{M}_{\odot}. \quad (3)$$

In our assumed cosmology, the velocity dispersion of Cl1216−1201 implies a mass of $\sim (1.2 \pm 0.3) \times 10^{15}\,\mathrm{M}_{\odot}$ which is somewhat higher than the X-ray and weak-lensing estimates. We note, however, that the spectroscopic estimate is derived from spectra obtained across the FORS FOV and therefore not directly comparable to the estimates derived within fixed radii.

4.1.4 Cl1216−1201: cluster AGN

75 X-ray point sources are identified in the Cl1216−1201 field, of which 12 lie within the FOV of the deep, multiband data. The multiband optical properties of these sources and the redshift estimates and probabilities of cluster membership returned by the photometric redshift codes are summarized in Table B4. None of the X-ray sources is a spectroscopically confirmed cluster member, but the four sources shown in Fig. 6 have optical properties which suggest that they may be AGN hosted by cluster members.

(i) Source Cl11216_X6 is firmly associated ($P_{\rm id} = 92$ per cent) with a spiral galaxy found 1′30″ from the cluster core which contains a very bright central point source. The source is not flagged as a possible cluster member based on photometric properties, but has a best-fitting redshift when fitted with a quasi-stellar object (QSO) template of $z_{\rm QSO} = 0.82$. The X-ray source has a full-band flux of $S_{0.5-8\,\mathrm{keV}} = 1.6 \times 10^{-14}$ and $HR = -0.12$, consistent with a moderately obscured AGN.

(ii) Similarly, source Cl1216_X8 is unambiguously associated with a galaxy found 3′30″ from the cluster centre containing a very bright AGN which is not flagged as a possible cluster member but has $z_{\rm QSO} = 0.72$. However, as the source lies outwith the FOV of the near-IR observations, the photometric redshift is based on only optical bands and is considered less reliable. The X-ray source has a full-band flux of $S_{0.5-8\,\mathrm{keV}} = 2.1 \times 10^{-14}$ and $HR = -0.50$, consistent with an unobscured AGN.

(iii) Source Cl1216_26 is ambiguously associated ($P_{\rm id} = 65$ per cent) with a galaxy lying 4 arcmin from the cluster centre which is flagged as a possible cluster member based on its photometric properties. However, like Cl1216_8, this source was not observed in the near-IR and its photometric redshift is based on only optical bands. As both photometric redshift codes prefer $z \sim 1.5$ solutions for this source and its optical counterpart is very faint, this source is most likely at a higher redshift than Cl1216.

(iv) Source Cl1216_X59, lies 3′20″ to the north-east of the cluster centre and is ambiguously identified with a group of three sources based on the WFI imaging. The *HST* view of this region reveals two fainter objects also within the X-ray 3σ error ellipse. The brightest source is flagged as possible cluster member based on its photometric properties. The X-ray detection has a flux $S_{0.5-8\,\mathrm{keV}} = 4.7 \times 10^{-15}$ and $HR = 0.36$, consistent with a heavily obscured AGN.

4.1.5 Cl1216-South

Unfortunately, the multiband imaging and FORS spectroscopy do not extend far enough to the south to confirm whether the collection of faint galaxies at the position of Cl1216-South are associated with the Cl1216−1201 structure at $z = 0.79$. The extension of the weak-lensing mass reconstruction along the NNE–SSW axis evident in Fig. 2 is suggestive, however, as is the indication of a similar elongation in the distribution of spectroscopically selected cluster

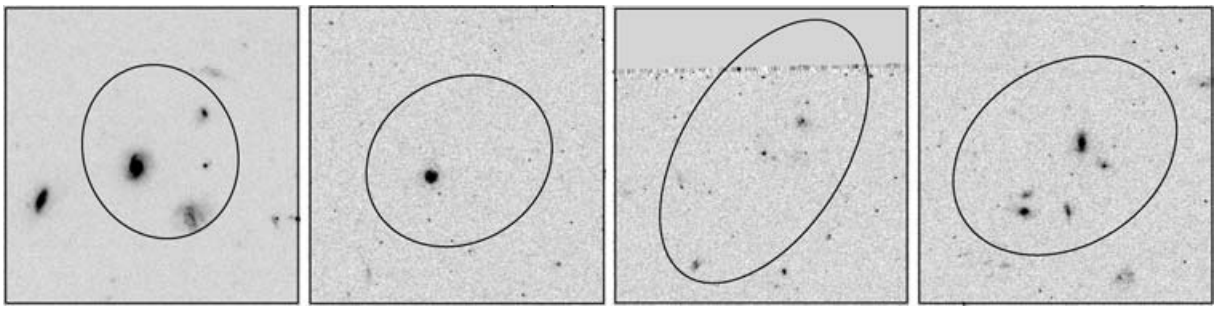

Figure 6. Candidate cluster AGN in Cl1216−1201. From left-hand side: Cl1216_X6, Cl1216_X8, Cl1216_X26, and Cl1216_X59. The boxes are 15 arcsec on a side, north is up, and east is to the left-hand side. The ellipses are the 3σ uncertainty of the *XMM* position.

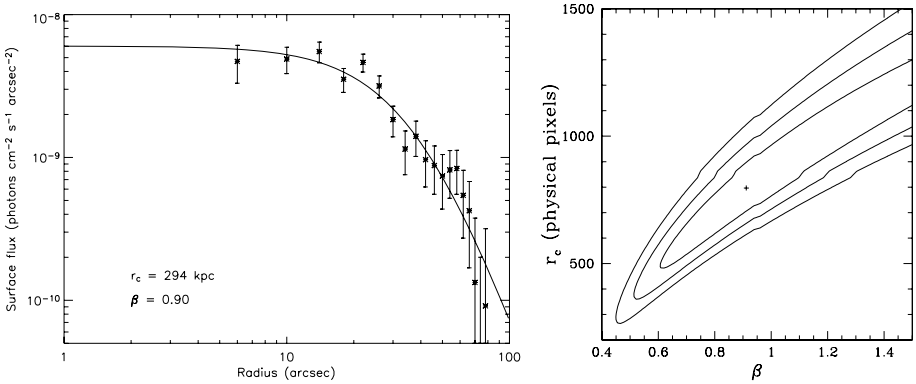

Figure 7. Left-hand panel: radial surface flux profile for Cl1216-South obtained by masking point sources and summing exposure-corrected, background-subtracted counts within annuli. Right-hand panel: corresponding constraints on β and r_c. The r_c axis is in *XMM* physical pixels which are 0.05 arcsec on a side. The contours mark 1, 2 and 3σ levels.

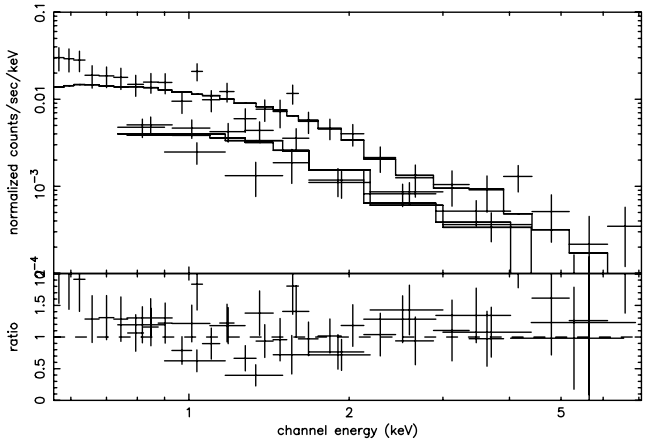

Figure 8. X-ray spectra of Cl1216-South extracted from the MOS (lower points) and pn (upper points) cameras and best-fitting thermal emission model (histograms). Residuals are shown in the lower panel.

members. While further spectroscopic observations will be necessary to determine the redshift of the Cl1216-South feature, we here include a discussion of its X-ray properties for completeness.

4.1.5.1 Cl1216-South: spatial analysis

A radially averaged surface flux profile was constructed from annuli centred on the estimated centre of the Cl1216-South emission ($\alpha = 12^{\rm h}16^{\rm m}39\overset{\rm s}{.}9, \delta = -12^\circ04'21''[J2000]$) as described in Section 3.2 and is shown in Fig. 7 (left-hand panel). The best-fitting parameters of a β-model fit are $\beta = 0.90^{+0.12}_{-0.09}$ and $r_c = 294^{+35}_{-35}$ kpc. The degeneracy between β and r_c is evident in confidence contours, however, which are plotted in Fig. 7 (right-hand panel) and indicate that the parameters are essentially unconstrained by this fit.

The Cl1216-South emission was modelled in two dimensions with a β-model plus a constant background level equal to that used in the fit to the main emission. The best-fitting model is centred on $\alpha = 12^{\rm h}16^{\rm m}40\overset{\rm s}{.}50, \delta = -12^\circ04'25''21[J2000]$, is significantly elliptical ($e = 0.44$, $\theta = 0.83$), and yields $\beta = 0.48^{+0.10}_{-0.06}$ and $r_c = 79^{+81}_{-49}$ kpc. Again, these errors do not reflect the true uncertainty in these parameters due to the degeneracy between r_c and β. The variation between these values and those implied by the one-dimensional fit results from the ellipticity of the Cl1216-South emission. To test consistency of the two methods, we extracted a radially averaged surface flux profile from an image of the best-fitting two-dimensional model in the same way we extracted the surface-flux profile from the data. A fit to this profile yielded best-fitting parameters of $\beta = 0.87$ and $r_c = 271$ kpc which are entirely consistent with those found for the one-dimensional fit.

4.1.5.2 Cl1216-South: spectral analysis

We extracted spectra of the cluster emission for the three EPIC cameras within circles centred on $\alpha = 12^{\rm h}16^{\rm m}39\overset{\rm s}{.}90, \delta = -12^\circ04'21''12[J2000]$ with radii of 50 arcsec. This aperture yielded 1271 counts where 472 are expected from the background. Use of a less-conservative extraction region with a radius of 115 arcsec was also examined, and found to produce entirely consistent results.

The spectra, shown in Fig. 8, were fitted to an absorbed MEKAL model with the absorption fixed at the Galactic value of 4.1×10^{20} cm^{-2} and the metallicity fixed at 0.3 solar. Assuming Cl1216-South lies at $z = 0.79$, the best-fitting model (reduced $\chi^2 = 0.9$) yields a temperature of $5.0 \pm ^{1.8}_{1.3}$ keV, a full-band luminosity of $L_{0.5-8\,{\rm keV}} = 1.7 \pm 0.2 \times 10^{44}$ erg s^{-1} cm^{-2}, and a bolometric luminosity of $L_{\rm bol} = 2.0 \pm 0.3 \times 10^{44}$ erg s^{-1} cm^{-2} within the spectral extraction radius. If the one-dimensional β profile derived above correctly describes the radial shape at large radii, the spectral radius encloses 68 per cent of the emission and the total luminosity of the southern component is $\sim 3 \times 10^{44}$ erg s^{-1} cm^{-2}.

4.2 Cl1054−1145

Cl1054−1145 at $z = 0.70$ contains 49 spectroscopically confirmed members with a velocity dispersion of 589^{+78}_{-70} km s^{-1} (Halliday et al. 2004), a well-developed red sequence, and a population of bluer galaxies (White et al. 2005). There is no evidence of substructure in the three-dimensional distribution of galaxies, but the lensing map of this cluster indicates that a large amount of mass may be currently infalling to the cluster (Clowe et al. 2006).

4.2.1 Cl1054−1145: spatial analysis

We overlay adaptively smoothed X-ray contours on an *I*-band image of the central region of the Cl1054−1145 field in Fig. 9. Extremely faint diffuse emission is visible at the observation aim-point, coincident with a concentration of spectroscopically confirmed cluster galaxies including the BCG. The diffuse emission is significantly

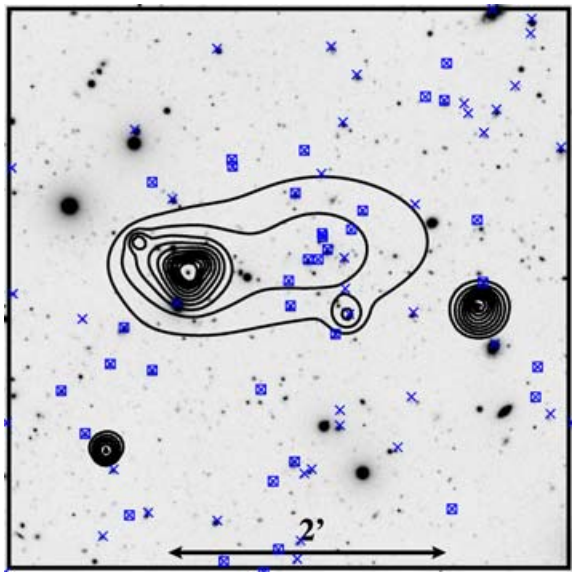

Figure 9. X-ray contours overlaid on an *I*-band image of the central region of the Cl1054−1145 field. The crosses indicate sources for which spectra have been obtained; the squares indicate spectroscopically confirmed cluster members. North is up and east is to the left-hand side.

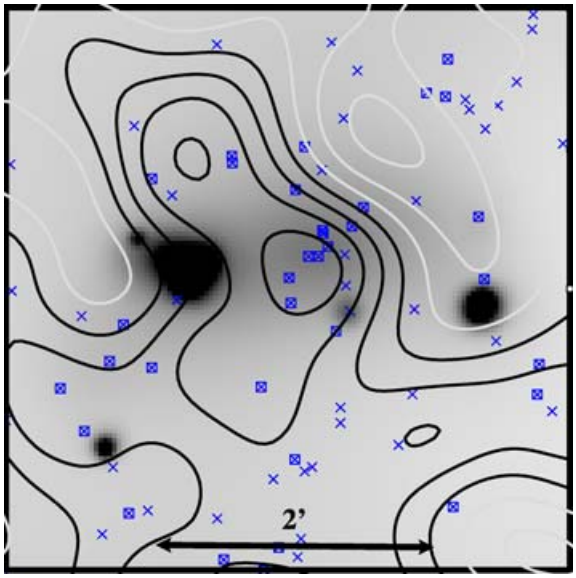

Figure 10. Adaptively smoothed 0.5–8 keV X-ray image of the central region of the Cl1054−1145 field with the Clowe et al. (2006) weak-lensing mass reconstruction of the field overlaid. Contour intervals are $\sim 1 \times 10^8$ $M_\odot$ kpc^{-2} relative to the local mean, with negative contours shown in light grey. The crosses indicate sources for which spectra have been obtained; the squares indicate spectroscopically confirmed cluster members. North is up and east is to the left-hand side.

contaminated by a bright point source ∼1 arcmin to the east of the aim-point, which appears to be an AGN associated with a faint galaxy known not to be a cluster member. A second bright point source lies ∼1 arcmin to the south-west and may be an AGN associated with the cluster (see Section 4.2.4). A third faint peak is visible in the adaptively smoothed image ∼20 arcsec to the south of the peak of the diffuse emission which, if not an artefact of the smoothing process, may indicate very faint emission associated with a background galaxy at $z = 0.76$. The diffuse X-ray contours, where they are not contaminated by point-source emission, appear to be somewhat elongated along the east–west axis. Mass contours from the Clowe et al. (2006) weak-lensing mass reconstruction are plotted over an image of the smoothed X-ray flux in Fig. 10 and indicate a significant mass peak coincident with the diffuse X-ray emission.

In Fig. 11, we show the radially averaged surface flux profile centred on the peak of the smoothed emission at $\alpha = 10^{\rm h}54^{\rm m}24\overset{\rm s}{.}8$, $\delta = -11^\circ 46' 21''$[*J*2000], which we fit to a β-model as above. The best-fitting parameters are $\beta = 1.09^{+0.39}_{-0.31}$ and $r_{\rm c} = 370^{+116}_{-77}$ kpc though, again, the confidence contours indicate that the degeneracy between the parameters renders them essentially unconstrained. Assuming a typical $\beta = 0.7$, this fit implies $r_{\rm c} \simeq 256^{+71}_{-57}$ kpc and suggests that the cluster may be less centrally concentrated than is typical. Further study of the morphology of the diffuse emission, including two-dimensional modelling, was not possible due to the faintness of the source and the proximity of the bright point sources.

4.2.2 Cl1054−1145: spectral analysis

X-ray spectra were extracted within a 50 arcsec radius centred on the peak of the smoothed emission from point-source free event lists in which an additional region was excised around the faint peak visible to the south of the cluster emission in the smoothed image. The aperture yielded 814 counts where 412 are expected from the background. Based on the properties of the bright point sources and the Medium Accuracy model of the *XMM* PSF, we estimate that 10–15 per cent of the extracted counts may be contamination from the wings of the brighter sources.

The spectra were fitted to an absorbed MEKAL model with the absorption fixed at the Galactic value of 3.5×10^{20} cm^{-2} and the metallicity fixed at 0.3 solar. The best-fitting model (reduced $\chi^2 = 1.4$) is plotted over the data in Fig. 12 and yields a temperature of $3.5^{+1.7}_{-1.6}$ keV, a full-band luminosity of $L_{0.5-8\,{\rm keV}} = 0.7 \pm 0.2 \times 10^{44}$ erg s^{-1} cm^{-2}, and a bolometric luminosity of $L_{\rm bol} = 0.8 \pm 0.2 \times 10^{44}$ erg s^{-1} cm^{-2} within the spectral extraction radius. Assuming the best-fitting values of β and $r_{\rm c}$ derived above, the spectral radius encloses 69 per cent of the cluster emission and the total luminosity of Cl1054−1145 is $\sim 1.2 \times 10^{44}$ erg s^{-1} cm^{-2}. Adopting the $\beta \equiv 0.7$ profile, the fraction of enclosed flux falls to 48 per cent of the emission and the total luminosity rises to $\sim 1.7 \times 10^{44}$ erg s^{-1} cm^{-2}.

4.2.3 Cl1054−1145: mass estimate

Taking our derived values of β, $r_{\rm c}$, and T at face value and adopting equation (2), the estimated mass of Cl1054−1145 within 1 Mpc is $\sim 3.8 \times 10^{14}$ $M_\odot$. Assuming that the $\beta \equiv 0.7$ profile discussed above yields a somewhat lower mass of $\sim 2.6 \times 10^{14}$ $M_\odot$, these X-ray-derived estimates are both in agreement with the weak-lensing estimate of $3.7^{+0.8}_{-0.9} \times 10^{14}$ $M_\odot$ though somewhat higher than the spectroscopically derived value of $\sim 1.2 \times 10^{14}$ $M_\odot$. However, we note that all of the derived X-ray properties are subject to large uncertainty due to the poor statistical quality of the data and the unquantified contamination by the nearby point sources. It is also far from clear if the assumptions underpinning equation (2) – spherical symmetry, hydrostatic equilibrium, and isothermality – hold in Cl1054−1145.

4.2.4 Cl1054−1145: cluster AGN

Of the 67 X-ray point sources detected in the Cl1054−1145 field, nine sources fall within the FORS FOV and three sources, shown

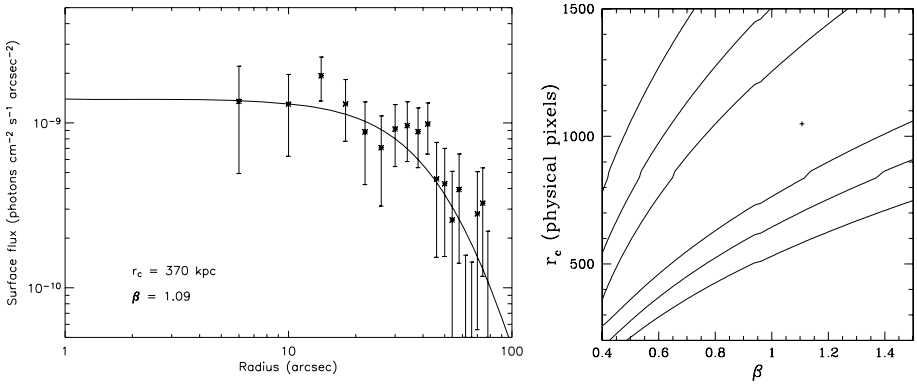

Figure 11. Left-hand panel: radial surface flux profile for Cl1054−1145 obtained by masking point sources and summing exposure-corrected, background-subtracted counts within annuli. Right-hand panel: corresponding constraints on β and r_c. The r_c axis is in *XMM* physical pixels which are 0.05 arcsec on a side. The contours mark 1, 2 and 3σ levels.

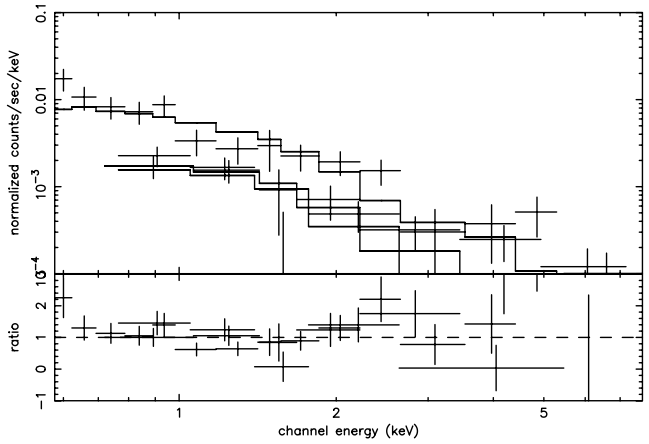

Figure 12. X-ray spectra of Cl1054−1145 extracted from the MOS (lower points) and pn (upper points) cameras and best-fitting thermal emission model (histograms). Residuals are shown in the lower panel.

in Fig. 13, have optical properties plausibly consistent with cluster membership.

(i) Source Cl1054_X9 is ambiguously associated with two galaxies located ∼4 arcmin south-east of the BCG. The probability of association $P_{\rm id}$, is roughly 50 per cent for both galaxies. The galaxy farther to the south is given very low membership probabilities ($P_{\rm mem} < 2$ per cent), whereas the northern galaxy is a spectroscopically confirmed cluster member with no obvious AGN signatures in its optical spectra. The X-ray detection has a flux $S_{0.5-8\,\rm keV} = 8.5 \times 10^{-14}$ erg s^{-1} cm^{-2} and $HR = 0.02$, consistent with a moderately obscured AGN.

(ii) Source Cl1054_X10, the compact source embedded in the eastern side of the diffuse emission, is unambiguously identified with a galaxy with a bright AGN core which lies ∼1 arcmin from the BCG and is flagged as a cluster candidate ($P_{\rm mem} \sim 75$ per cent). The X-ray detection has a flux $S_{0.5-8\,\rm keV} = 5.4 \times 10^{-14}$ erg s^{-1} cm^{-2} and $HR = 0.5$, consistent with an unobscured AGN. However, as it is likely that the optical colours are affected by the luminous AGN, the validity of the photometric redshift based on a galaxy template is questionable. $z_{\rm QSO}$ for this source is ∼1.5.

(iii) Source Cl1054_X26 is unambiguously associated with a galaxy ∼3′45″ from the cluster centre which is flagged as a possible cluster member, though with fairly low probability ($P_{\rm mem} \sim$ 30 per cent). The source has disturbed morphology and is faint in both the optical and X-ray bands, with an X-ray flux of $S_{0.5-8\,\rm keV} = 7.2 \times 10^{-15}$ erg s^{-1} cm^{-2} and $HR = 0.36$, consistent with a heavily obscured AGN.

4.3 Cl1040−1155

There are 30 spectroscopically identified cluster galaxies in the Cl1040−1155 field at $z = 0.70$ with the second lowest velocity dispersion in the EDisCS high-redshift sample, $\sigma = 418^{+55}_{-46}$ km s^{-1}. Isopleths of galaxy density show a clear concentration around the BCG (White et al. 2005), but no significant mass peak is detected in the weak-lensing analysis which yields an upper limit on the mass which is consistent with the low velocity dispersion (Clowe et al. 2006).

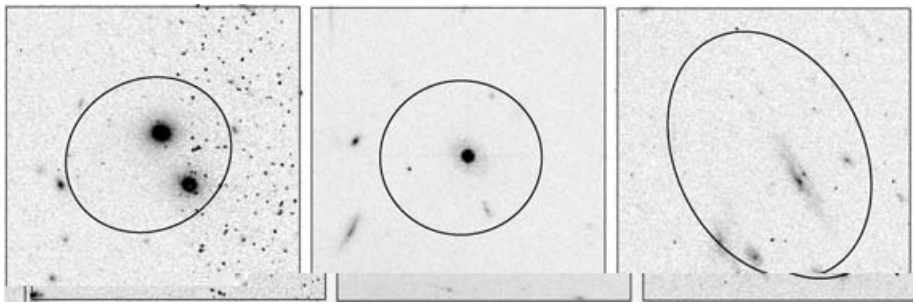

Figure 13. Candidate cluster AGN in Cl1054−1145. From left-hand side: Cl1054_X9, Cl1054_X10, and Cl1054_X26. The boxes are 15 arcsec on a side, north is up, and east is to the left-hand side. The ellipses are the 3σ uncertainty of the *XMM* position.

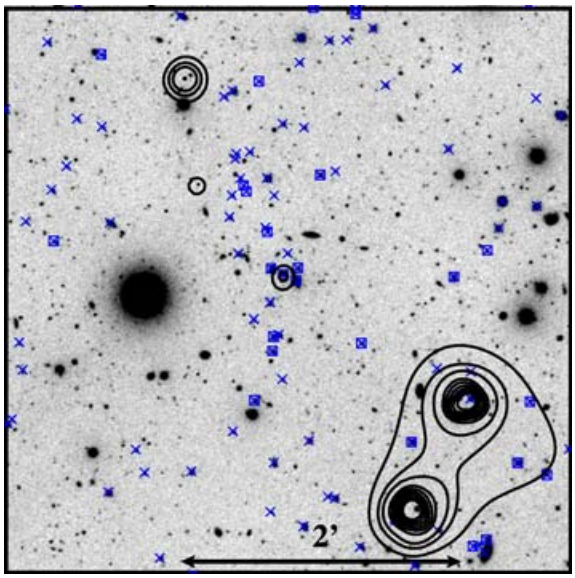

Figure 14. X-ray contours overlaid on an *I*-band image of the central region of the Cl1040−1155 field. The crosses indicate sources for which spectra have been obtained; the squares indicate spectroscopically confirmed cluster members. North is up and east is to the left-hand side.

4.3.1 Cl1040−1155: spatial analysis

In Fig. 14, we show an *I*-band image of the central region of the Cl1040−1155 field overlaid with contours of adaptively smoothed X-ray flux. There is no evidence for extended X-ray emission associated with the ICM. An extremely faint compact source is seen at the observation aim-point which appears to be associated with one of the spectroscopically confirmed cluster members near to the BCG. The source was not detected by the wavelet detection algorithm; it may not meet the selected significance or total counts thresholds or it may be an artefact of the adaptive smoothing. A radially averaged surface flux profile centred on the aim-point of the *XMM* observation is shown in Fig. 15. It is well fitted with a constant background level and confirms the lack of diffuse detection. The data place a 3σ upper limit on diffuse emission on 0.5 Mpc scales of 0.2×10^{44} erg s^{-1}.

Neither of the two marginal peaks detected in the weak-lensing mass reconstruction is coincident with the position of the BCG, as

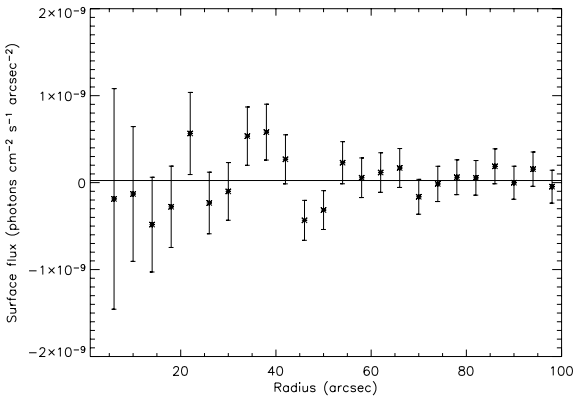

Figure 15. Radial surface flux profile for Cl1054−1145 obtained by masking point sources and summing exposure-corrected, background-subtracted counts within annuli.

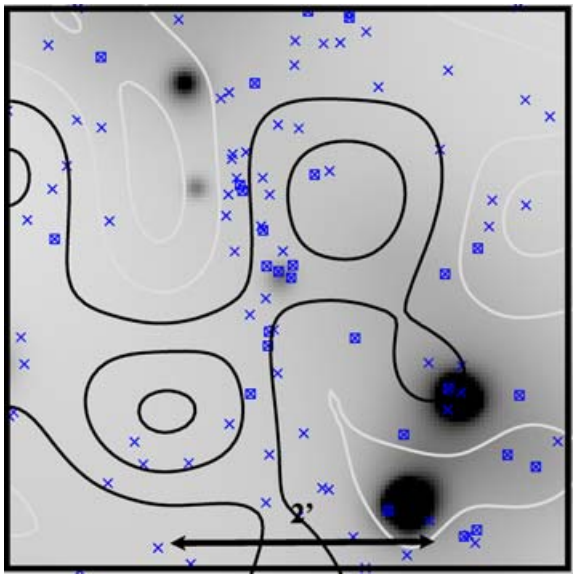

Figure 16. Adaptively smoothed 0.5–8 keV X-ray image of the central region of the Cl1040−1155 field with the Clowe et al. (2006) weak-lensing mass reconstruction of the field overlaid. Contour intervals are $\sim 1 \times 10^8$ M$_\odot$ kpc^{-2} relative to the local mean, with negative contours shown in light grey. The crosses indicate sources for which spectra have been obtained; the squares indicate spectroscopically confirmed cluster members. North is up and east is to the left-hand side.

shown in Fig. 16. That Cl1040−1155 is not detected in the X-ray and only marginally detected in the weak-lensing analysis suggests that the overdensity of galaxies at $z = 0.70$ in the field comprises a poor cluster or a group, (see also discussion in White et al. 2005).

4.3.2 Cl1040−1155: cluster AGN

11 of the 67 X-ray sources detected in the Cl1040−1155 field fall within the FORS FOV. Three of these, shown in Fig. 17, have optical properties plausibly consistent with cluster membership.

(i) Source Cl1040_X12 is ambiguously associated with two objects $\sim 1'30''$ from the cluster core. The object to the west is a star, and is selected as the WFI counterpart to the X-ray source by the association algorithm. However, a spectroscopically confirmed cluster member visible farther to the east in the *HST* image is also within the 3σ error circle. The X-ray detection has a flux $S_{0.5-8\,\mathrm{keV}} = 4.0 \times 10^{-14}$ erg s^{-1} cm^{-2} and $HR = 0.03$, which is consistent with a moderately obscured AGN and unusually hard for stellar X-ray emission.

(ii) Source Cl1040_X23 is unambiguously identified with a galaxy $\sim 2'30''$ from the cluster centre which is flagged as a possible cluster member based on its photometric properties, though with low membership probabilities ($P_{\mathrm{mem}} \sim 25$ per cent). The X-ray flux of the source is $S_{0.5-8\,\mathrm{keV}} = 1.1 \times 10^{-14}$erg s^{-1} cm^{-2} and $HR = 0.07$, consistent with a moderately obscured AGN.

(iii) Source Cl1040_X67 is ambiguously associated with two sources $\sim 4'15''$ from the cluster centre. The source farther to the north is extremely faint, whereas the southern source is flagged as a possible cluster member. The photometry for this source is based on only optical colours, however, and is therefore considered not reliable. The X-ray flux of the source is $S_{0.5-8\,\mathrm{keV}} = 3.7 \times 10^{-14}$erg s^{-1} cm^{-2} and $HR = 0.03$, consistent with a moderately obscured AGN.

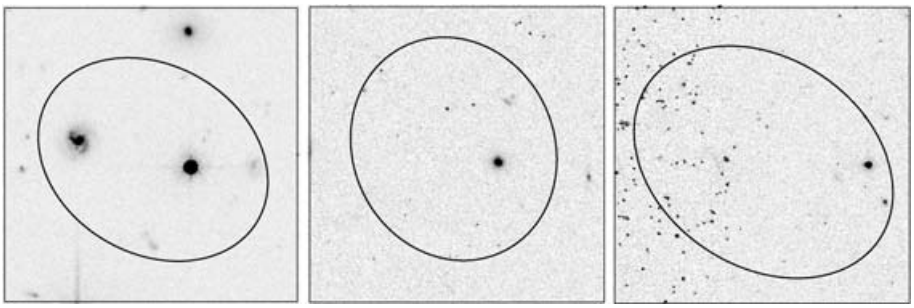

Figure 17. Candidate cluster AGN in Cl1040−1155. From left-hand side: Cl1040_X12, Cl1040_X23 and Cl1040_X67. The boxes are 15 arcsec on a side, north is up, and east is to the left-hand side. The ellipses are the 3σ uncertainty of the *XMM* position.

Table 4. Summary of the X-ray properties of EDisCS clusters and the Cl1216-South structure. The columns are slope and core radius of the best-fitting surface brightness models, ellipticity, radius of the spectral aperture, source counts within the aperture, background counts within the aperture, X-ray temperature, 0.5–8 keV flux within the aperture, 0.5–8 keV luminosity within the aperture, and total bolometric luminosity. β and r_c are from one-dimensional modelling except for Cl1216-South, where the two-dimensional model is preferred. Total luminosities are extrapolated from the spectral radius, using the parameters of the best-fitting one-dimensional β-models. Core radii are given in kpc, temperatures in keV, fluxes in 10^{-14} erg s^{-1} cm^{-2} and luminosities in 10^{44} erg s^{-1}. The quoted errors indicate 90 per cent confidence levels; the errors on β and r_c underestimate the true uncertainty due to the strong degeneracy of these parameters (see Figs 3, 7 and 11).

Source	β	r_c	e	r_s	C_{src}	C_{bkg}	kT	$S_{0.5-8}$	$L_{0.5-8}$	L_{bol}
Cl1216−1201	$0.68^{+0.06}_{-0.05}$	159^{+20}_{-18}	0.0	40″	1503	194	$4.8^{+0.8}_{-0.7}$	$8.8^{+0.6}_{-0.6}$	$2.5^{+0.2}_{-0.2}$	∼5
Cl1054−1145	0.7	256^{+71}_{-57}	–	50″	814	412	$3.5^{+1.7}_{-1.6}$	$6.1^{+0.8}_{-0.6}$	$0.7^{+0.2}_{-0.2}$	∼2
Cl1040−1155	–	–	–	–	–	–	–	< 0.8	< 0.2	< 0.3
Cl1216-South	$0.48^{+0.10}_{-0.06}$	79^{+81}_{-49}	0.4	50″	1271	472	$5.0^{+1.8}_{-1.3}$	$3.2^{+0.6}_{-0.6}$	$1.7^{+0.2}_{-0.2}$	∼3

5 CLUSTER SCALING RELATIONS

The X-ray properties of the three EDisCS targets and the southern component in the Cl1216−1201 field are summarized in Table 4. In Figs 18–20, we compare the X-ray and optical properties of these structures with the best-fitting scaling relations of Xue & Wu (2000), derived from a standardized sample of 274 primarily low-redshift clusters taken from the literature. The Xue & Wu (2000) sample spans a range in redshift from $0.005 < z < 1$, but ∼65 per cent are

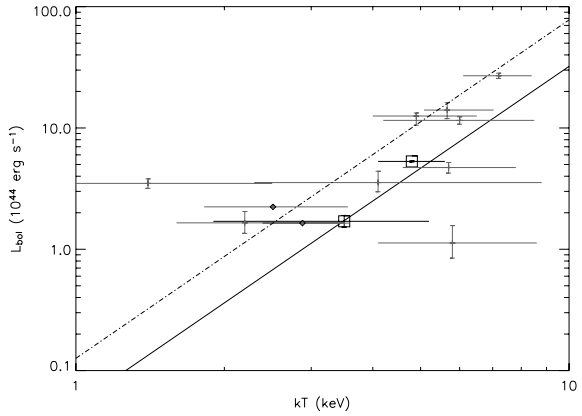

Figure 18. X-ray temperature versus bolometric X-ray luminosity for the Cl1216−1201 and Cl1054−1145 clusters (squares). The solid line shows the best-fitting relation of Xue & Wu (2000), whereas the dashed line indicates this relation evolved to $z = 0.8$, following the parametrization of Vikhlinin et al. (2002). The points denoted by small diamonds are the optically selected $z = 0.76$ and 0.90 clusters of Lubin et al. (2004), whereas other points are the X-ray-selected $0.6 < z < 1.4$ clusters of Mullis et al. (2005), Gioia et al. (2004), Donahue et al. (1999), Gioia et al. (1999), Stanford et al. (2001) and Valtchanov et al. (2004).

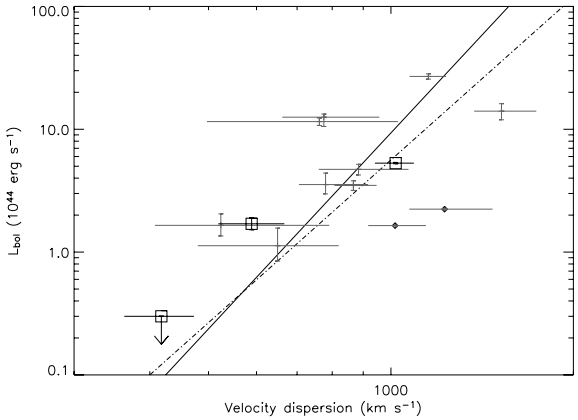

Figure 19. Bolometric X-ray luminosity versus optical velocity dispersion for the Cl1216−1201, Cl1054−1145, and Cl1040−1155 clusters. The symbols are as described in Fig. 18. The Cl1040−1155 point is a 3σ detection limit based on the background level within a radius of 90 arcsec. The solid line shows the best-fitting relation of Xue & Wu (2000), whereas the dotted line shows that of Mahdavi & Geller (2001). In addition to the optically selected clusters of Lubin et al. (2004), RX J1716.6+6708 (Gioia et al. 1999, $z = 0.81$) also appears significantly underluminous in X-rays for its velocity dispersion.

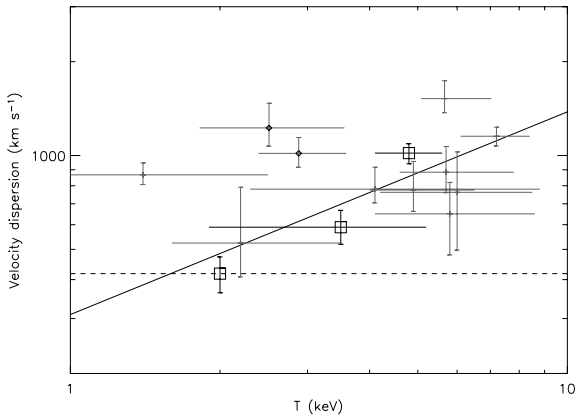

Figure 20. Optical velocity dispersion versus X-ray temperature for in the Cl1216−1201, Cl1054−1145, and Cl1040−1155 clusters. The symbols are as described in Fig. 18. As Cl1040−1155 was undetected in the *XMM* observations, its temperature is unknown as indicated by the dashed line. The solid line shows the best-fitting relation of Xue & Wu (2000) and other data points are as in Fig. 18. In addition to the optically selected clusters of Lubin et al. (2004), the X-ray-selected clusters RX J1716.6+6708 (Gioia et al. 1999, $z = 0.81$) and XLSSC001 (Valtchanov et al. 2004, $z = 0.61$) appear to have low X-ray temperatures for their velocity dispersions.

at $z < 0.1$, and <2 per cent are at $z > 0.4$. We have converted these relations from an Einstein–deSitter cosmology to the concordance ΛCDM cosmology assuming a mean redshift $\bar{z} = 0.1$. For comparison at high redshift, we have drawn from the literature a sample of clusters with $0.6 < z < 1.4$ for which X-ray temperature, X-ray luminosity and optical velocity dispersion are known (Donahue et al. 1999; Gioia et al. 1999; Stanford et al. 2001; Gioia et al. 2004; Lubin et al. 2004; Valtchanov et al. 2004; Mullis et al. 2005). Of these, only the two Lubin et al. (2004) clusters at $z = 0.76$ and 0.90 are optically selected. We have standardized the plotted values where necessary by calculating bolometric luminosities from a MEKAL model with the appropriate temperature and an abundance of 0.3 solar. Where luminosities are given within a radius, we have accounted for flux outside the aperture using the best-fitting β-model, when given, or a typical profile ($\beta = 0.7$, $r_c = 140$ kpc).

In Fig. 18, we plot bolometric X-ray luminosity versus X-ray temperature for Cl1216−1201 and Cl1054−1145 along with the comparison sample of high-redshift clusters. We compare these points with both the Xue & Wu (2000) L_X–T relation and its evolution to $z = 0.8$ following the parametrization of Vikhlinin et al. (2002): $L(T, z) = L(T) \times (1 + z)^{1.5\pm0.3}$. Both detected EDisCS sources are consistent at the 90 per cent confidence level with the relation of Xue & Wu, and appear slightly underluminous compared with the evolved relation. The scatter among the plotted high-redshift clusters is substantial, however, and the X-ray properties of the EDisCS clusters, like those of the Lubin et al. (2004) optically selected clusters, are fully consistent with the properties of the X-ray-selected sample as a whole.

We note that the values of L_X and T derived for the Cl1216-South structure, assuming it is associated with Cl1216 at $z = 0.79$ are also consistent with the Xue & Wu (2000) relation. While we stress that further observations are needed to determine the true redshift of this source and therefore do not include it in Fig. 18, we note that fits to the Cl216-South spectra yield values which are consistent with this relation within the 90 per cent confidence limits only if the assumed redshift is $z > 0.7$, with assumed $0.1 < z < 0.6$ fits producing values which are severely underluminous for the implied temperatures in comparison with the Xue & Wu (2000) relation.

In Fig. 19, we plot the bolometric X-ray luminosity versus optical velocity dispersion for the targetted EDisCS clusters over both the best-fitting Xue & Wu (2000) L_X–σ relation and that of Mahdavi & Geller (2001). The variation between these two relations may result from the inclusion of lower-mass groups in the Mahdavi & Geller cluster sample which are fitted with a separate, shallower relation in the Xue & Wu paper. The Cl1216−1201 and Cl1054−1145 points lie near to the low-redshift relations and within the scatter of the other high-redshift points. Cl1216−1201 is underluminous for its velocity dispersion with respect to the Xue & Wu (2000) relation by roughly a factor of 2, but is entirely consistent with the Mahdavi & Geller (2001) relation. The non-detection of Cl1040−1155 is potentially consistent with either of the low-redshift relations, as it places an upper limit on the luminosity which is roughly twice that expected from them.

In contrast, and despite their unremarkable position on the L_X–T plot, the optically selected clusters of Lubin et al. (2004) stand well apart from both the low-redshift L_X–σ relations and the bulk of the high-redshift clusters in Fig. 19, exhibiting significantly lower X-ray luminosities than those expected for their velocity dispersions. The

umino85(bolomfican.5943 51n.5943ity)-it The.436.8(TJ1716+6708,.436.8(T236cr

intracluster light rather than excess galaxy counts – and X-ray surveys may effectively identify the more fully virialized structures at high redshift. The apparent lack of evolution in the cluster scaling relations for these structures suggests that these detection techniques are well suited for selection of relaxed, high-redshift clusters whose ICM is in place and stable by $z \sim 0.8$. That the X-ray determined masses of Cl1216−1201 and Cl1054−11, derived under the assumption that they are relaxed structures in hydrostatic equilibrium, are in general agreement with those determined from the weak-lensing analysis lends further support to this conclusion.

These first results also suggest that the discrepancy which has been noted between other optically selected, high-redshift cluster samples and the X-ray luminous cluster population may not be due to a peculiarity of X-ray selection. Rather, as has been suggested, optical matched-filter techniques may preferentially select a physically distinct population of massive structures at high redshift. Both Lubin et al. (2004) and Bower et al. (1997) argued that the discrepancy between the high velocity dispersion and low X-ray luminosity of their optically selected clusters could be explained were they systems of lower virial temperature undergoing gravitational collapse. Similarly, Hicks et al. (2004) noted that the X-ray properties of their sample of RCS clusters – less centrally condensed morphologies and low X-ray temperatures and luminosities which none the less lie on the L_X –T relationship of the general cluster population – are consistent with their containing relatively low-mass virialized cores imbedded within larger forming structures. It is interesting to note in this context that RX J1716.6+6708 – the only X-ray-selected cluster with ICM properties mimicking those of the optically selected clusters in Figs 20 and 19 – is also believed to be in the process of collapsing.

6.2 Cluster AGN

In addition to the diffuse ICM emission, these data have allowed us to begin compiling a sample of candidate cluster AGN in the EDisCS sample. Though no cluster AGN are yet spectroscopically confirmed, cross-correlation of the X-ray catalogues with the multiband data available over the central $\sim 3 \times \sim 3$-Mpc^2 region of each cluster field has identified several promising candidates. The extant data indicate a maximum of three to four cluster AGN per field. The candidates are found ∼0.5–1.5 Mpc from the cluster cores and, if associated with the clusters, comprise a sample of variously obscured Type I and II AGN with luminosities of $L_{0.5-8\,\mathrm{keV}} = 10^{42-43}$ erg s^{-1}. While spectroscopic confirmation of candidate cluster AGN and extension of this preliminary study to our larger sample will both be necessary to characterize the AGN content of the EDisCS clusters in a rigorous way, it is interesting that the preliminary data on these first clusters suggest that their AGN populations are typical of those found in the X-ray luminous cluster population in general. In a study of over 100 clusters at $0.1 < z < 1$ selected from the *Chandra* archive, X-ray luminous clusters were found to host two to three AGN on average, at distances of 0.5–1 Mpc from the cluster centre (Dowsett 2006). Further study of the cluster AGN population within EDisCS will be conducted when planned X-ray and radio observations of the remainder of the sample are available.

7 SUMMARY

In this paper, we have presented *XMM–Newton* observations of three optically selected, high-redshift clusters which comprise the first results of an X-ray survey of the full EDisCS $z > 0.6$ sample. We find Cl1216−1201 at $z = 0.79$ to have a relaxed X-ray morphology, a temperature of $T = 4.8^{+0.8}_{-0.7}$ keV, and a bolometric X-ray luminosity of $\sim 5 \times 10^{44}$ erg s^{-1} cm^{-2}. We detect a second diffuse X-ray source 3.5 arcmin to the south-west which, if also at $z = 0.79$, has a similar temperature and a somewhat lower luminosity. We marginally detect Cl1054−1145 at $z = 0.70$ and derive a temperature of $T = 3.5^{+1.7}_{-1.6}$ keV and a bolometric luminosity of $\sim 2 \times 10^{44}$ erg s^{-1} cm^{-2}. Cl1040−1155 at $z = 0.70$ is not detected in our 30-ks *XMM* exposure; on a scale of 0.5 Mpc diameter, we place a 3σ upper limit on its luminosity of $L_{0.5-8} < 0.2 \times 10^{44}$ erg s^{-1}.

In both X-ray-detected clusters, the diffuse X-ray emission is coincident with galaxy overdensities containing the cluster BCG and peaks in the weak-lensing mass reconstructions of the field. Furthermore, mass estimates based on the X-ray data for Cl1216−1201 and Cl1054−1145 are comparable to those derived from the lensing analysis. Despite evidence of some level of extended substructure in mass maps, velocity dispersion histograms, and – in the Cl1216−1201 field – the possible detection of a second X-ray component, the multiband evidence is suggestive of relatively relaxed systems in which the galaxies and the ICM are in virial equilibrium within the same potential well. We stress, however, that these conclusions are based on only two cluster detections, one of which is of poor statistical quality, and require confirmation in further, deeper observations of the remainder of the sample.

Comparison of the X-ray source-lists with the multiband photometry and spectroscopy has identified several promising candidate cluster AGN, though none are yet spectroscopically confirmed. We have identified three to four candidates per field; if associated with the target clusters, they comprise a population of Type I and Type II objects with typical X-ray luminosities of $L_{0.5-8\,\mathrm{keV}} = 10^{42-43}$ erg s^{-1} residing 0.5–1.5 Mpc from the cluster centres. As reported in Dowsett (2006), these findings are typical of X-ray luminous clusters.

The principal result of this preliminary work is the consistency of our optically selected clusters with both the low-redshift X-ray/optical scaling relations and the X-ray-selected cluster population at high redshift. This result stands in contrast to the disparate X-ray/optical properties reported for optically selected high-redshift clusters in the literature, which appear systematically cooler and less luminous than expected for their velocity dispersions. This early analysis suggests that the EDisCS, like surveys based on X-ray luminosity, may effectively select virialized high-redshift clusters in which the ICM is already well formed and stable by $z \sim 0.8$. The discrepancy between the X-ray/optical properties of our sample and those of previously reported high-redshift clusters selected using optical matched-filter techniques may result from the latter being less fully virialized structures still undergoing collapse.

Our results suggest that X-ray surveys may provide an unbiased view of virialized massive clusters at high redshift, but also stress the need for surveys in both optical and X-ray bands to fully sample the mass distribution at epochs where massive clusters are still forming. The planned extension of this study to the full EDisCS high-redshift sample with deeper X-ray exposures will allow us to confirm these preliminary results and also to extend the high-redshift L_X–σ and T–σ relations to much lower velocity dispersions. The EDisCS sample may offer a unique opportunity to target virialized structures at high redshift which are intrinsically similar to the X-ray luminous population but with lower masses which are more representative of the precursors of common present-day clusters.

ACKNOWLEDGMENTS

This work is based on observations collected at the European Southern Observatory, Chile, as part of large programme 166. A-0162 (the ESO Distant Cluster Survey). OJ acknowledges PPARC for support through a Postdoctoral Fellowship and thanks Michael Brown for helpful discussions. PB acknowledges the Royal Society for support through its University Research Fellowship Scheme. The authors thank the anonymous referee for a careful and helpful review of the draft.

REFERENCES

Arnaud M. et al., 2002, A&A, 390, 27
Basilakos S., Plionis M., Georgakakis A., Georgantopoulos I., Gaga T., Kolokotronis V., Stewart G. C., 2004, MNRAS, 351, 989
Bolzonella M., Miralles J.-M., Pelló R., 2000, A&A, 363, 476
Bower R. G., Bohringer H., Briel U. G., Ellis R. S., Castander F. J., Couch W. J., 1994, MNRAS, 268, 345
Bower R. G., Castander F. J., Ellis R. S., Couch W. J., Boehringer H., 1997, MNRAS, 291, 353
Cash W., 1979, ApJ, 228, 939
Castander F. J., Ellis R. S., Frenk C. S., Dressler A., Gunn J. E., 1994, ApJ, 424, L79
Clowe D. et al., 2006, A&A, 451, 395
Donahue M., Voit G. M., Scharf C. A., Gioia I. M., Mullis C. R., Hughes J. P., Stocke J. T., 1999, ApJ, 527, 525
Donahue M. et al., 2001, ApJ, 552, L93
Donahue M. et al., 2002, ApJ, 569, 689
Dowsett R., 2006, PhD thesis, Edinburgh University
Evrard A. E., Metzler C. A., Navarro J. F., 1996, ApJ, 469, 494
Finn R. A. et al., 2005, ApJ, 630, 206
Freeman P. E., Kashyap V., Rosner R., Lamb D. Q., 2002, ApJS, 138, 185
Gehrels N., 1986, ApJ, 303, 336
Gioia I. M., Maccacaro T., Schild R. E., Wolter A., Stocke J. T., Morris S. L., Henry J. P., 1990, ApJS, 72, 567
Gioia I. M., Henry J. P., Mullis C. R., Ebeling H., Wolter A., 1999, AJ, 117, 2608
Gioia I. M., Wolter A., Mullis C. R., Henry J. P., Böhringer H., Briel U. G., 2004, A&A, 428, 867
Gladders M. D., Yee H. K. C., 2005, ApJS, 157, 1
Gonzalez A. H., Zaritsky D., Dalcanton J. J., Nelson A., 2001, ApJS, 137, 117
Gonzalez A. H., Zaritsky D., Simard L., Clowe D., White S. D. M., 2002, ApJ, 579, 577
Green P. J. et al., 2004, ApJS, 150, 43
Halliday C. et al., 2004, A&A, 427, 397
Hicks A., Ellingson E., Bautz M., Yee H., Gladders M., Garmire G., 2005, Adv. Space Res., 36, 706
Holden B. P., Romer A. K., Nichol R. C., Ulmer M. P., 1997, AJ, 114, 1701
Johnson O., Best P. N., Almaini O., 2003, MNRAS, 343, 924
Kaastra J. S., 1992, An X-Ray Spectral Code for Optically Thin Plasmas (Internal SRON-Leiden Report, updated version 2.0)
Liedahl D. A., Osterheld A. L., Goldstein W. H., 1995, ApJ, 438, L115
Lubin L. M., Mulchaey J. S., Postman M., 2004, ApJ, 601, L9
Lumb D. H., Warwick R. S., Page M., De Luca A., 2002, A&A, 389, 93
Mahdavi A., Geller M. J., 2001, ApJ, 554, L129
Martini P., Kelson D., Kim D., Mulchaey J., Athey A., 2006, ApJ, 644, 116
Mewe R., Lemen J. R., van den Oord G. H. J., 1986, A&AS, 65, 511
Mewe R., Gronenschild E. H. B. M., van den Oord G. H. J., 1985, A&AS, 62, 197
Mullis C. R., Rosati P., Lamer G., Böhringer H., Schwope A., Schuecker P., Fassbender R., 2005, ApJ, 623, L85
Nevalainen J., Markevitch M., Lumb D., 2005, ApJ, 629, 172
Pierre M., 2003, IAUJD, 10, 31
Plionis M., Basilakos S., Georgantopoulos I., Georgakakis A., 2005, ApJ, 622, L17
Poggianti B. M. et al., 2006, ApJ, 642, 188
Postman M., Lubin L. M., Gunn J. E., Oke J. B., Hoessel J. G., Schneider D. P., Christensen J. A., 1996, AJ, 111, 615
Read A. M., Ponman T. J., 2003, A&A, 409, 395
Romer A. K., Viana P. T. P., Liddle A. R., Mann R. G., 2001, ApJ, 547, 594
Rosati P., della Ceca R., Norman C., Giacconi R., 1998, ApJ, 492, L21
Rudnick G. et al., 2001, AJ, 122, 2205
Rudnick G. et al., 2003, ApJ, 599, 847
Rutledge R. E., Brunner R. J., Prince T. A., Lonsdale C., 2000, ApJS, 131, 335
Stanford S. A., Holden B., Rosati P., Tozzi P., Borgani S., Eisenhardt P. R., Spinrad H., 2001, ApJ, 552, 504
Sutherland W., Saunders W., 1992, MNRAS, 259, 413
Valtchanov I. et al., 2004, A&A, 423, 75
Vikhlinin A., VanSpeybroeck L., Markevitch M., Forman W. R., Grego L., 2002, ApJ, 578, L107
White S. D. M. et al., 2005, A&A, 444, 365
Xue Y.-J., Wu X.-P., 2000, ApJ, 538, 65

SUPPLEMENTARY MATERIAL

The following supplementary material is available for this article online:

Appendix A: X-ray point-source catalogues.

Appendix B: Candidate optical counterparts.

This material is available for download as part of the full-text version of the article from http://www.blackwell-synergy.com.

This paper has been typeset from a TEX/LATEX file prepared by the author.